Pumping and Mixing in Active Pores

G. C. Antunes,[1,2,3,*] P. Malgaretti,[1,2,3,†] J. Harting,[3,4] and S. Dietrich[1,2]
[1]Max–Planck–Institut für Intelligente Systeme, Heisenbergstraße 3, 70569 Stuttgart, Germany
[2]IV. Institut für Theoretische Physik, Universität Stuttgart, Pfaffenwaldring 57, 70569 Stuttgart, Germany
[3]Helmholtz-Institut Erlangen-Nürnberg für Erneuerbare Energien (IEK–11), Forschungszentrum Jülich, Cauerstraße 1, 91058 Erlangen, Germany
[4]Department Chemie—und Bioingenieurwesen und Department Physik, Friedrich-Alexander-Universität Erlangen-Nürnberg, Fürther Straße 248, 90429 Nürnberg, Germany

(Received 18 March 2022; accepted 14 September 2022; published 25 October 2022)

We show both numerically and analytically that a chemically patterned active pore can act as a micro- or nanopump for fluids, even if it is fore-aft symmetric. This is possible due to a spontaneous symmetry breaking which occurs when advection rather than diffusion is the dominant mechanism of solute transport. We further demonstrate that, for pumping and tuning the flow rate, a combination of geometrical and chemical inhomogeneities is required. For certain parameter values, the flow is unsteady, and persistent oscillations with a tunable frequency appear. Finally, we find that the flow exhibits convection rolls and hence promotes mixing in the low Reynolds number regime.

DOI: 10.1103/PhysRevLett.129.188003

The manipulation of fluid flow at the micro- and nanometer scale has currently attracted the attention of a large scientific community [1–4]. Indeed, the emerging techniques of micro- and nanofluidics have been applied successfully to the synthesis of microparticles, to the transport of biomaterials, and to the functioning of chemical reactors [5–7]. Such techniques have been exploited in biomedical research to study and manipulate biological tissues, and to develop both new drugs and means of delivering them [8–12]. Similarly, inkjet printing, a common technique for 3D fabrication, requires fluids to be pumped through channels with a diameter of ∼50–80 μm [13–15]. Moreover, lab-on-a-chip setups have been employed both in medical research [16–18] as well as in clinical diagnosis and treatment [4,9]. In all these situations, a fluid needs to be pumped in a controlled fashion, making micropumps a basic component of many microfluidic systems [8,19]. In addition, controlling chemical reactions within such microfluidic devices requires the stirring of solutions by means of micromixers [20,21]. As the cross sections of the channels are reduced, surface and finite size effects become more relevant and can be exploited for designed microfluidic applications [22–27].

From this perspective, phoretic phenomena [28] can provide an intriguing technique to manipulate fluid flows in a micro- and nanochannel or pore. In particular in diffusioosmosis, inhomogeneous densities of certain components of the solution set up local pressure imbalances in the vicinity of solid walls, hence leading to the onset of a net fluid flow [28]. One way of inducing such local pressure gradients at steady-state is to fabricate chemically or geometrically inhomogeneous pores [29–31]. A similar procedure has already been exploited for colloids and led to the realization of self-phoretic Janus particles [32–38]. For these colloids net motion is attained because half of their surface is covered with a catalyst promoting a chemical reaction which in turn is responsible for the inhomogeneous density of reaction products along the surface of the colloid. Interestingly, even colloids homogeneously covered with catalyst can swim due

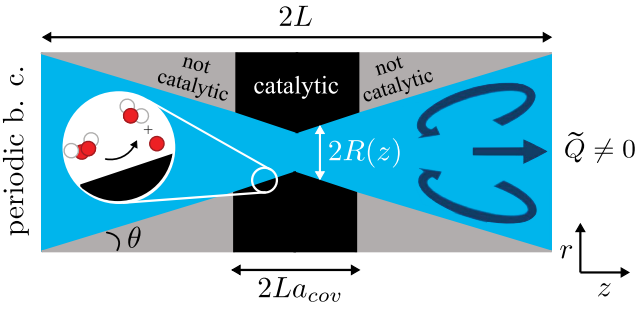

FIG. 1. Longitudinal section of the axially symmetric and partially active pore with length $2L$ and variable radius $R(z)$. The decomposition of a chemical species to produce solute occurs solely in the catalytically active part of the inner pore wall with length $2La_{cov}$ (black). Convection rolls (dark blue arrows) appear due to diffusioosmosis and eventually may lead to the onset of a net nonzero flow rate $\tilde{Q}$.

to an instability triggered when the transport of solute by advection is comparable to that due to diffusion [39,40].

In this Letter, we show that diffusiophoresis within inhomogeneously chemically patterned pores can lead to the onset of spontaneous symmetry breaking (pumping), oscillations, and mixing. By means of both numerical simulations and analytical modeling we show that the onset of these regimes is controlled by three dimensionless parameters: the Péclet number (controlling the role of advection), the chemical patterning (controlling the surface inhomogeneity), and the corrugation (controlling the geometrical inhomogeneity).

In particular, as reported [41,42] previously, pumping does not occur for pores with homogeneous (constant) cross sections or for pores with chemically homogeneous surface properties. In addition, beyond the stationary Stokes limit, the steady flow becomes unstable and we observe the onset of an "inertial phoresis" regime characterized by sustained oscillations, the frequency of which can be tuned upon varying the extent of the catalytic coverage of the pore. In all cases, convection rolls emerge, which can be exploited as so-called micromixers [20,43].

In the following, we consider hourglass-shaped pores, see Fig. 1, which are axially symmetric with respect to the z axis and symmetric with respect to the plane $z = 0$ in the center (fore-aft symmetry). The pore is defined by its length $2L$, its maximum radius $R_{\max}$, and its opening angle θ (Fig. 1). Thus, the spatially varying radius $R(z)$ is given by

$$R(z) = R_{\max}(\theta) - \tan(\theta)(L - |z|). \tag{1}$$

Upon a change of θ, $R_{\max}$ is adjusted in order to approximately conserve the volume of the pore. The pore is filled with a Newtonian fluid, the dynamics of which is governed by the Navier-Stokes equation with no-slip boundary conditions on the pore walls. The surface of the pore is patterned with a catalytic coating in the section $z \in \{-a_{\mathrm{cov}}L, a_{\mathrm{cov}}L\}$, where the covering fraction a_{cov} can vary from zero (no coating) to one (full coating). Such a catalytic coating enables a chemical reaction resulting in the local synthesis of reaction products, which in the following are summarily called "solute." The solute is decomposed homogeneously in the bulk fluid with rate χ (with dimension sec^{-1}). In order to keep the model simple, we assume that the number densities of the reactants are kept constant in time and homogeneous in space, and that the number density ρ of the solute is much smaller than the number densities of the fluid molecules such that effectively it can be regarded as an ideal gas. The effective interaction potential U_{wall} between the solute molecules and the pore walls is assumed to be a piecewise linear function of the distance r from the wall,

$$U_{\mathrm{wall}}(r) = \begin{cases} U_0(1 - r/l) & 0 \le r \le l, \\ 0 & l \le r, \end{cases} \tag{2}$$

where l is the range of U_{wall}. It is assumed to be much smaller than the average radius of the pore $R_0 = R_{\max} - \tan(\theta)L/2$. The overdamped dynamics of the solute number density is governed by the Smoluchowski equation,

$$\dot{\rho} = -\nabla \mathbf{j} - \chi\rho, \qquad \mathbf{j} = -D\nabla\rho - \beta D\rho\nabla U_{\mathrm{wall}} + \boldsymbol{v}\rho, \tag{3}$$

where D is the diffusion coefficient of the solute, $\beta = 1/(k_B T)$ is the inverse thermal energy, $\boldsymbol{v}$ is the velocity field of the solution, and χ is an empirical input parameter with the unit sec^{-1}. Equations (3) obey periodic boundary conditions on the ends of the pore segment and flux boundary conditions on the surface of the pore,

$$\mathbf{j} \cdot \mathbf{n}|_{[z,\phi,r=R(z)]} = \begin{cases} \xi, & |z| < La_{\mathrm{cov}}, \\ 0, & \text{otherwise}, \end{cases} \tag{4}$$

where ϕ is the azimuthal angle, $\mathbf{n}$ is a unit vector perpendicular to the pore wall (pointing towards the inside of pore), and ξ is a positive constant with dimension $[\mathrm{m}^2\ \mathrm{s}]^{-1}$.

The wall-solute interaction results in a laterally inhomogeneous pressure along the wall, hence coupling Eq. (3) with the Navier-Stokes equation and the continuity equation for the fluid density (see Supplemental Material [44]). These three equations are solved in parallel using a finite-difference solver for the first one (second order in space and first order in time), and the lattice Boltzmann method (LBM) [45–47] for the other two ones. (Details of the numerical implementation can be found in Ref. [48].)

In the following, we report all quantities in units of the pore length $2L$ (40 spatial lattice units), and of the fluid relaxation time $\tau_f = (2L)^2/\nu$ (9600 temporal lattice units), which is the time required for momentum to diffuse across the pore in the longitudinal dimension, with ν being the kinematic viscosity (1/6 in lattice units).

By following Ref. [48], in all simulations we have used parameter values as reported in the caption of Fig. 2. We remark that there is a maximum value of θ for which the bottleneck of the pore is shut down. This value is obtained by numerically solving for $\theta_{\max}$ such that $R(z = 0; \theta = \theta_{\max}) = 0$. For the geometry under consideration, this value amounts to $\theta_{\max} \approx 0.4\pi$. The system is initialized with the fluid at rest and with a fore-aft asymmetric density profile of the solute. Since the effective interaction potential is repulsive, the flow field resulting from the initial one is directed from the solute-poor half of the pore to the solute-rich half [28] [see Figs. 2(a) and 2(b)]. The competition between advective and diffusive transport is key to the dynamics we report. This competition is quantified by the Péclet number $\mathrm{Pe} = v^* L/D$ which is proportional to the characteristic velocity v^* and sets the ratio of the timescales of diffusive and advective transport. Since it is possible to vary Pe by varying any of the three quantities, due to numerical efficiency, we varied Pe by tuning the diffusion coefficient. Only the solute inside the thin region around the pore walls

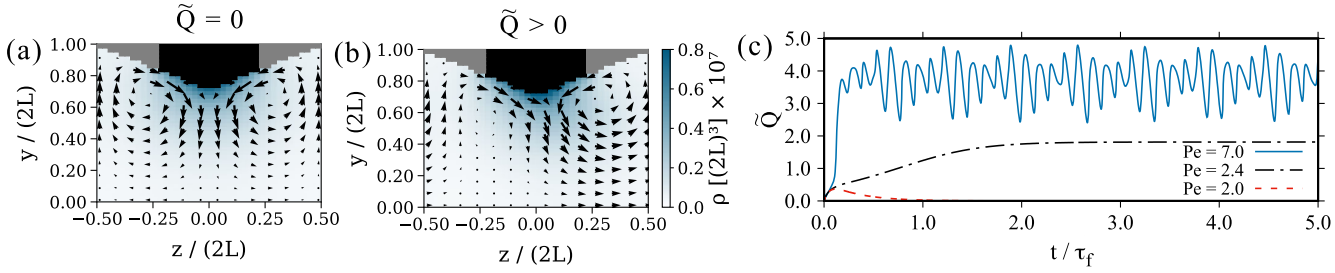

FIG. 2. Panels (a) and (b), snapshots of the steady-state velocity profile in the plane $x = 0$ for Pe $= 2.0$ and 2.4, respectively. (c) Flow rate $\tilde{Q}$ as a function of time, with $a_{\mathrm{cov}} = 0.45$. The parameters are $R_{\max}/(2L) = 1$, $\nu\tau_f/(2L)^2 = 1$, $\beta U_0 = 4 \times 10^{-4}$, $l/(2L) = 0.1$, $\xi(2L)^2\tau_f = 1.5 \times 10^7$, and $\chi\tau_f = 9.6$. In lattice units: $L = 20$, $\eta = 1/6$, $U_0 = 4 \times 10^{-4}$, $l = 4$, $\xi = 1$, $\chi = 10^{-3}$, $\beta = 1$, and $\theta = \pi/6$. The simulation box is of size $80 \times 80 \times 40$.

where $U_{\mathrm{wall}} \neq 0$ contributes to diffusioosmosis. Therefore, we focus on the transport in this region. The characteristic velocity v^* is estimated from the numerical simulations by averaging the velocity of the fluid close to the pore walls (see Supplemental Material) for the cases in which pumping occurs, which yields $v^* = 1.3$ (0.0056 in lattice units).

For sufficiently small values of Pe the flow field relaxes to a steady state characterized by convection rolls [Fig. 2(a)], which act to mix the fluid. These states are characterized also by a vanishing fluid flow rate

$$\tilde{Q} = \frac{\tau_f}{(2L)^3} \int_0^{R(z)} dr\, r \int_0^{2\pi} d\phi\, v_z(r, \phi, z) \qquad (5)$$

[see the dashed line in Fig. 2(c)], which we report normalized by $(2L)^3/\tau_f$. However, upon increasing the value of Pe, we observe a nonvanishing steady-state fluid flow rate, $\tilde{Q} \neq 0$ [Figs. 2(b) and 2(c)]. In these steady states, the advection of solute compensates for the diffusion which attempts to equilibrate the solute density in both the fore and the aft half of the pore. As the convection rolls are present also in these pumping states, the channel mixes and pumps the fluid at the same time.

Figure 3(a) shows the dependence of $\tilde{Q}$ on Pe, and it highlights the presence of a crossover value of Pe_c above which pumping (i.e., $\tilde{Q} \neq 0$) occurs. The values of both Pe_c and $\tilde{Q}$ are sensitive to the chemical and geometrical properties of the pore. Indeed, Fig. 3(b) shows that pumping is suppressed in the limits of small ($a_{\mathrm{cov}} \to 0$) and large (in this case $a_{\mathrm{cov}} \gtrsim 0.8$) chemical patterns, respectively. In particular, we have found no pumping steady state in the case of a pore fully covered with catalyst ($a_{\mathrm{cov}} = 1$). The onset of pumping is sensitive to the geometry of the pore, too. In fact, Fig. 3(c) shows that there are both lower and upper limits $\theta_{\min} < \theta < \theta_{\max}$ below and above which pumping does not occur. This is in contrast to what has been (theoretically) reported for colloidal particles which undergo a spontaneous symmetry breaking also in the case of homogeneous surface properties. Figure 3 clearly shows that the three dimensionless parameters (Pe, a_{cov}, θ) which we have identified play a crucial role in the onset of the spontaneous symmetry breaking. Therefore the rich phenomenology that we report here cannot be attained for low Péclet numbers (no advection), homogenous chemical patterning (small and large values of a_{cov}), and for flat or very corrugated channels (small and large values of θ).

Remarkably, there is a regime (solid symbols in Fig. 3), with $\mathrm{Pe} > \mathrm{Pe}^{\mathrm{osc}}$, $a_{\mathrm{cov}} > a_{\mathrm{cov}}^{\mathrm{osc}}$, and $\theta > \theta^{\mathrm{osc}}$, in which $\tilde{Q}$ exhibits sustained oscillations about a nonvanishing flow, rather than converging towards a steady state [see the full line in Fig. 2(c)]. These sustained oscillations are qualitatively different from those observed in Ref. [42] which occur at zero pumping rate. Here, the pulsatilelike flow arises from a negative feedback loop which works as follows. An initial increase in $\tilde{Q}$ causes the solute to be advected away from the center of the pore at a rate faster than the rate at which the catalysis at the wall can replace it. This results in a large amount of solute (which we denote as a plume) which is rapidly ejected from the wall (see video

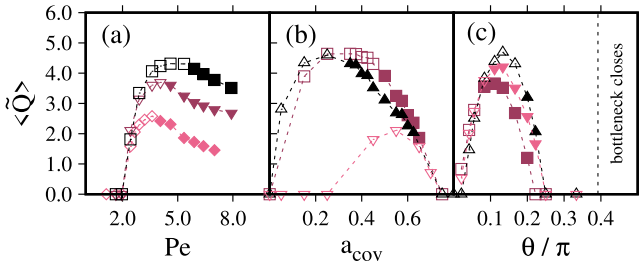

FIG. 3. Time-averaged flow rate $\langle\tilde{Q}\rangle$. Open (solid) symbols mark systems which converge to a steady state (limit cycle). $\langle\tilde{Q}\rangle$ (a) as function of Pe for $\theta = \pi/6$ and for $a_{\mathrm{cov}} = \{0.45$ (squares), 0.55 (inverted triangles), 0.65 (diamonds)$\}$; (b) as function of a_{cov} for $\theta = \pi/6$ and for Pe $= \{2.4$ (inverted triangles), 5.3 (squares), 8.0 (triangles)$\}$; (c) as function of θ, for $\{\mathrm{Pe}, a_{\mathrm{cov}}\} = [\{5.3, 0.45\}$ (triangles), $\{8.0, 0.45\}$ (inverted triangles), $\{8.0, 0.55\}$ (squares)]. For further parameters see the caption of Fig. 2. In panel (c), the size of the simulation box is adjusted so as to keep the volume of the pore constant. The dashed lines are guides to the eye.

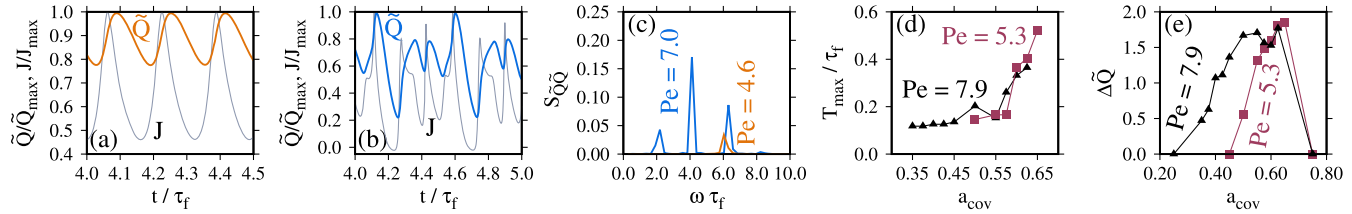

FIG. 4. In panels (a) and (b) $\tilde{Q}$ and J [thick lines (orange, blue), and grey thin lines, respectively] normalized by their maximum value. In (a) $\{a_{\mathrm{cov}}, \mathrm{Pe}\} = \{0.55, 4.6\}$ and in (b) $\{a_{\mathrm{cov}}, \mathrm{Pe}\} = \{0.55, 7.0\}$. (c) Power spectrum $S_{\tilde{Q}\,\tilde{Q}}$ of $\tilde{Q}(t)$ [from panels (a) and (b)]. (d) Period of oscillations T_{max} in units of τ_f. (e) Amplitude of the oscillations $\Delta\tilde{Q}$. For (d) and (e), the data are shown as function of a_{cov} for $\mathrm{Pe} = \{5.3$ (squares), 7.9 (triangles)$\}$. For further parameters see the caption of Fig. 2.

in the Supplemental Material). The depletion of solute from the center of the hourglass causes the flow J of the solute, i.e.,

$$J = \int_0^{R(0)} dr\, r \int_0^{2\pi} d\phi\, v_z(r, \phi, z = 0)\rho(r, \phi, z = 0) \qquad (6)$$

to be reduced even as $\tilde{Q}$ increases. This eventually triggers a decrease in the asymmetry of the solute between each half of the pore. Eventually, $\tilde{Q}$ is diminished, even though the center of the pore repopulates with solute, and the solute flow J increases. This delay between $\tilde{Q}$ and J is visible in Figs. 4(a) and 4(b), and is a result of the nonzero relaxation time $\tau_f = (2L)^2/\nu$ of the fluid velocity distribution. Accordingly, the sustained oscillations occur when the fluid velocity cannot adiabatically follow the solute density field. This latency triggers an instability and prevents relaxation to a steady state.

Interestingly, the onset of sustained oscillations roughly coincides with the regime in which the time-averaged flow rate $\langle\tilde{Q}\rangle$ diminishes upon an increase in Pe, i.e., upon favoring even further advection with respect to diffusion [Fig. 3(a)]. Such a nonmonotonic dependence of $\tilde{Q}$ on Pe is reminiscent of the one observed for both isotropic and Janus colloids [39,49,50]. To further characterize the sustained oscillations of $\tilde{Q}$, we analyze their Fourier spectra ($S_{\tilde{Q}\,\tilde{Q}}$, see Supplemental Material). Figure 4(c) shows rich power spectra with multiple excited modes. In order to analyze the dependence of the power spectra on the extent a_{cov} of the chemical pattern, and on Pe, we focus on the period T_{max} associated with that frequency for which the power spectrum attains its maximum: $2\pi\tau_f/T_{\mathrm{max}}$. The dependence of T_{max} on a_{cov}, normalized by the relaxation time of the fluid, is plotted in Fig. 4(d). In general, larger values of a_{cov} result in larger values of T_{max}, but all values remain comparable to (but less than) the relaxation time of the fluid. Accordingly, the period of the oscillations is shorter than the relaxation time of the fluid, hence preventing the relaxation of the fluid velocity towards a steady state. Concerning the amplitude of the oscillations, Fig. 4(e) shows that larger values of a_{cov} lead to larger amplitudes $\Delta\tilde{Q} = (\tilde{Q}_{\mathrm{max}} - \tilde{Q}_{\mathrm{min}})/2$, defined as one half of the difference between the maximum, $\tilde{Q}_{\mathrm{max}}$, and the minimum, $\tilde{Q}_{\mathrm{min}}$, value of $\tilde{Q}$ (i.e., to larger plumes). Interestingly, the comparison of Figs. 4(d) and 4(e) tells that larger periods T_{max} are associated with larger amplitudes of the oscillations as both increase upon increasing a_{cov}. This different behavior on both sides of the oscillatory regime implies that the transition to oscillations from the side of smaller values of a_{cov} is of a different kind as compared to the one which occurs upon approaching it from the side of larger values of a_{cov}. Indeed, in the former case, the amplitude of the oscillations grows smoothly from $\Delta\tilde{Q} = 0$, i.e., a supercritical Hopf bifurcation occurs [51]. In contrast, upon approaching from large values of a_{cov} ($a_{\mathrm{cov}} \gtrsim 0.65$), the amplitude of the oscillations suddenly jumps from $\Delta\tilde{Q} = 0$ to $\Delta\tilde{Q} \neq 0$ (i.e., oscillations in $\tilde{Q}$), i.e., a subcritical Hopf bifurcation occurs [51].

Finally, in Fig. 5, we report on the asymptotic dynamics as a function of two out of the three dimensionless parameters identified in Fig. 3, namely, Pe and a_{cov} for a given value of the corrugation $\theta = \pi/6$. In particular, we observe a minimum value of Pe below which there is no pumping ($\tilde{Q} = 0$) for any value of a_{cov} and that $a_{\mathrm{cov}} \approx 0.5$ maximizes the range of Pe values for which pumping occurs. Interestingly, Fig. 5 shows that not only pumping (see Fig. 3), but also oscillations occur for a specific range of values of Pe and a_{cov} (in the present case θ is fixed). In order to understand the onset of pumping, we develop a

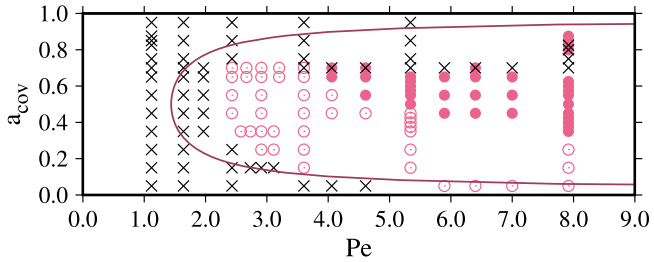

FIG. 5. Classification of the asymptotic dynamics into non-pumping states (crosss), steady pumping states (circles), and oscillating states (filled circles). Overlapping symbols indicate bistability (see Supplemental Material). The purple line is a semianalytic prediction for the onset of pumping. (Concerning the parameter set, see the caption of Fig. 2.)

semianalytical approach based on the Fick-Jacobs equation [52–54]. Within this approach, we couple Eq. (3), which governs the dynamics of the solute, to the stationary Stokes equation in the case of weakly varying pores for which we can apply the lubrication approximation (see Supplemental Material). Without any fitting parameter, the theory semi-quantitatively reproduces the onset of pumping described by the condition $\Delta\Omega(\mathrm{Pe}, a_{\mathrm{cov}}) = 0$, where the function $\Delta\Omega(\mathrm{Pe}, a_{\mathrm{cov}})$ is given by the right-hand side of Eq. (S71) of the Supplemental Material. This approach captures the corresponding values of $\mathrm{Pe}_{\mathrm{on}}(a_{\mathrm{cov}})$, as well as the two values of $a_{\mathrm{cov}}^{\mathrm{on}}$ associated with a given value of Pe.

The typical experimental realization of phoresis relies on hydrogen peroxide decomposed by platinum. In such a setup, the role of the solute is played by oxygen, which has a diffusion coefficient of $D \approx 10^3\ \mu\mathrm{m}^2\,\mathrm{s}^{-1}$. This setup generates flows with characteristic velocities $v^* \lesssim 10\ \mu\mathrm{ms}^{-1}$ [55]. According to our results, for a symmetric active pore with $a_{\mathrm{cov}} \approx 0.5$, pumping occurs for $\mathrm{Pe} \approx 1$, and therefore for $L \approx 10^2 - 10^3\ \mu\mathrm{m}$. The fluid relaxation time for an aqueous solution ($\nu \approx 10^6\ \mu\mathrm{m}^2\,\mathrm{s}^{-1}$) in this pore is $\tau_f \approx 10^{-2} - 1$ s, and so we expect the oscillations to have a frequency in the order of $1/\tau_f \approx 1$–100 Hz.

By means of both numerical simulations and analytical modeling, we have shown that diffusioosmosis inside pores can lead to spontaneous symmetry breaking and sustained oscillations of the flow rate. In particular, our results show that the spontaneous symmetry breaking occurs when three conditions are met simultaneously: large Péclet number ($\mathrm{Pe} \gtrsim 1$), inhomogeneous chemical patterning ($a_{\mathrm{cov}} \neq 0$, 1), and mild channel corrugation ($0 < \theta < \theta_{\mathrm{max}}$). The oscillations, which resemble a pulsatile flow, appear as an additional instability, occurring at higher values of Pe than the spontaneous symmetry breaking leading to steady pumping. They occur if the magnitude of a_{cov} lies between two "critical" values, one showing a subcritical and the other one a supercritical Hopf bifurcation. In particular, the frequency of these oscillations can be tuned hence paving the way for the design of a phoretic microfluidic oscillator [56]. Interestingly, the three functionalities of the active pore (mixer, pump, oscillator) can be enabled via a_{cov} which may be varied by changing the light source shining on the pore in the case in which the pore is coated by a photoactivated catalyst [57].

P. M. and J. H. acknowledge funding by the Deutsche Forschungsgemeinschaft (DFG, German Research Foundation)—Project-ID 416229255—SFB 1411 and Project-ID 431791331—SFB 1452.

*g.antunes@fz-juelich.de
†p.malgaretti@fz-juelich.de

[1] T. M. Squires and S. R. Quake, Rev. Mod. Phys. **77**, 977 (2005).
[2] G. M. Whitesides, Nature (London) **442**, 368 (2006).
[3] J. Novotný and F. Foret, J. Sep. Sci. **40**, 383 (2017).
[4] X. Hou, Y. S. Zhang, G. T. Santiago, M. M. Alvarez, J. Ribas, S. J. Jonas, P. S. Weiss, A. M. Andrews, J. Aizenberg, and A. Khademhosseini, Nat. Rev. Mater. **2**, 17016 (2017).
[5] I. Shestopalov, J. D. Tice, and R. F. Ismagilov, Lab Chip **4**, 316 (2004).
[6] K. Amreen and S. Goel, ECS J. Solid State Sci. Technol. **10**, 017002 (2021).
[7] T. Bailey, M. Pinto, N. Hondow, and K.-J. Wu, MethodsX **8**, 101246 (2021).
[8] Y.-N. Wang and L.-M. Fu, Microelectron. Eng. **195**, 121 (2018).
[9] Y. Yang, Y. Chen, H. Tang, N. Zong, and X. Jiang, Small Methods **4**, 1900451 (2020).
[10] Q. Ma, H. Ma, F. Xu, X. Wang, and W. Sun, Microsyst. Nanoeng. **7**, 19 (2021).
[11] E. Egrov, C. Pieters, H. Horach-Rechtman, J. Shklover, and A. Schroeder, Drug Deliv. Transl. Res. **11**, 345 (2021).
[12] X. Zhao, S. Liu, L. Yildirimer, H. Zhao, R. Ding, H. Wang, W. Cui, and D. Weitz, Adv. Funct. Mater. **26**, 2809 (2016).
[13] M. H. Warsi, M. Yusuf, M. Al Robaian, M. Khan, A. Muheem, and S. Khan, Curr. Pharm. Des. **24**, 4949 (2018).
[14] Y. Guo, H. Patanwala, B. Bognet, and A. Ma, Rapid Prototype J. **23**, 562 (2017).
[15] D. Lohse, Annu. Rev. Fluid Mech. **54**, 349 (2022).
[16] P. S. Dittrich and A. Manz, Nat. Rev. Drug Discov. **5**, 210 (2006).
[17] R. Pol, F. Céspedes, D. Gabriel, and M. Baeza, Trends Anal. Chem. **95**, 62 (2017).
[18] A. Francesko, V. F. Cardoso, and S. Lanceros-Méndez, in *Microfluidics for Pharmaceutical Applications: From Nano/Micro Systems Fabrication to Controlled Drug Delivery*, edited by H. A. Santos, D. Liu, and H. Zhang (William Andrew Publishing, Norwich, 2019), p. 3.
[19] D. J. Laser and J. G. Santiago, J. Micromech. Microeng. **14**, R35 (2004).
[20] A. D. Stroock, S. K. W. Dertinger, A. Ajdari, I. Mezić, H. A. Stone, and G. M. Whitesides, Science **295**, 647 (2002).
[21] G. Cai, L. Xue, H. Zhang, and J. Lin, Micromachines **8**, 274 (2017).
[22] L. Luo, D. A. Holden, and H. S. White, ACS Nano **8**, 3023 (2014).
[23] C. Zhao and C. Yang, Microfluid. Nanofluid. **13**, 179 (2012).
[24] H. S. Gaikwad, G. Kumar, and P. K. Mondal, Soft Matter **16**, 6304 (2020).
[25] S. Eloul and D. Frenkel, Soft Matter **17**, 1173 (2021).
[26] B. Abécassis, C. Cottin-Bizonne, C. Ybert, A. Ajdari, and L. Bocquet, New J. Phys. **11**, 075022 (2009).
[27] Z. Tan, M. Yang, and M. Ripoll, Phys. Rev. Appl. **11**, 054004 (2019).
[28] J. L. Anderson, Annu. Rev. Fluid Mech. **21**, 61 (1989).
[29] T. Yu, A. G. Athanassiadis, M. N. Popescu, V. Chikkadi, A. Güth, D. P. Singh, T. Qiu, and P. Fischer, ACS Nano **14**, 13673 (2020).
[30] S. Michelin and E. Lauga, Sci. Rep. **9**, 10788 (2019).
[31] S. Michelin, T. D. Montenegro-Johnson, G. De Canio, N. Lobato-Dauzier, and E. Lauga, Soft Matter **11**, 5804 (2015).

[32] J. R. Howse, R. A. L. Jones, A. J. Ryan, T. Gough, R. Vafabakhsh, and R. Golestanian, Phys. Rev. Lett. **99**, 048102 (2007).
[33] S. J. Ebbens and J. R. Howse, Soft Matter **6**, 726 (2010).
[34] C. Bechinger, R. Di Leonardo, H. Löwen, C. Reichhardt, G. Volpe, and G. Volpe, Rev. Mod. Phys. **88**, 045006 (2016).
[35] M. Safdar, J. Simmchen, and J. Jänis, Environ. Sci. **4**, 1602 (2017).
[36] M. J. Esplandiu, K. Zhang, J. Fraxedas, B. Sepulveda, and D. Reguera, Acc. Chem. Res. **51**, 1921 (2018).
[37] M. N. Popescu, W. E. Uspal, A. Domínguez, and S. Dietrich, Acc. Chem. Res. **51**, 2991 (2018).
[38] P. Malgaretti and J. Harting, Chem. Nano. Mat. **7**,1073 (2022).
[39] S. Michelin, E. Lauga, and D. Bartolo, Phys. Fluids **25**, 061701 (2013).
[40] P. de Buyl, A. S. Mikhailov, and R. Kapral, Europhys. Lett. **103**, 60009 (2013).
[41] S. Michelin, S. Game, E. Lauga, E. Keaveny, and D. Papageorgiou, Soft Matter **16**, 1259 (2020).
[42] Y. Chen, K. L. Chong, L. Liu, R. Verzicco, and D. Lohse, J. Fluid Mech. **919**, A10 (2021).
[43] A. Sarkar, A. Narvaez Salazar, and J. Harting, Microfluid. Nanofluid. **13**, 19 (2012).
[44] See Supplemental Material at http://link.aps.org/supplemental/10.1103/PhysRevLett.129.188003 for further details on the coupling of Navier-Stokes with the solute density, the definition of the power spectrum and the Péclet number, as well as the derivation of the semianalytic prediction for the onset of pumping.
[45] R. Benzi, S. Succi, and M. Vergassola, Phys. Rep. **222**, 145 (1992).
[46] T. Krüger, H. Kusumaatmaja, A. Kuzmin, O. Shardt, G. Silva, and E. Viggen, *The Lattice Boltzmann Method* (Springer, Berlin, 2017).
[47] H. Liu, Q. Kang, C. R. Leonardi, S. Schmieschek, A. Narváez, B. D. Jones, J. R. Williams, A. J. Valocchi, and J. Harting, Comput. Geosci. **20**, 777 (2016).
[48] T. Peter, P. Malgaretti, N. Rivas, A. Scagliarini, J. Harting, and S. Dietrich, Soft Matter **16**, 3536 (2020).
[49] S. Michelin and E. Lauga, J. Fluid Mech. **747**, 572 (2014).
[50] S. Michelin and E. Lauga, Eur. Phys. J. E **38**, 7 (2015).
[51] S. Strogatz, *Nonlinear Dynamics and Chaos* (CRC Press, Boca Raton, 2015).
[52] R. Zwanzig, J. Phys. Chem. **96**, 3926 (1992).
[53] D. Reguera and J. M. Rubi, Phys. Rev. E **64**, 061106 (2001).
[54] P. Malgaretti, I. Pagonabarraga, and J. Rubi, Front. Phys. **1**, 21 (2013).
[55] S. Ebbens, M.-H. Tu, J. R. Howse, and R. Golestanian, Phys. Rev. E **85**, 020401(R) (2012).
[56] S.-J. Kim, R. Yokokawa, and S. Takayama, Lab Chip **13**, 1644 (2013).
[57] J. Palacci, S. Sacanna, S.-H. Kim, G.-R. Yi, D. J. Pine, and P. M. Chaikin, Phil. Trans. R. Soc. A **372**, 20130372 (2014).